33RD CONGRESS
OF THE INTERNATIONAL COUNCIL
OF THE AERONAUTICAL SCIENCES
STOCKHOLM, SWEDEN, 4–9 SEPTEMBER, 2022

ICAS
2022
SWEDEN

DEVELOPMENT OF MULTI-CANARD UAV FOR ACTIVE AEROELASTIC CONTROL TOWARD PSEUDO-SMALL SATELLITES

Naoto Morita[1], Shinichi Nakasuka[1], Takeshi Tsuchiya[1],
Kazuki Takashima[1], Yasuyuki Taguchi[1], Kaito Suzuki[1],
Takashi Koyama[1], Ren Eto[1] & Ichiro Baba[1]

[1]The University of Tokyo, 7-3-1, Hongo, Bunkyo-ku, Tokyo, Japan

Abstract

The authors have analysed and flight-tested an aircraft with multiple canards to demonstrate active aeroelastic control, which actively changes the structural displacement of the wing. This paper describes this experimental aircraft's design, construction, and flight testing with multiple canards. In the design, a coupled structure-motion analysis was carried out. The results show that the aircraft with multiple canards is suitable for active aeroelastic control. To compare the active aeroelastic control analysis with the flight tests, the authors built this experimental aircraft with multiple canards with a span of 4 m. To capture structural displacements at high speed, an IMU was installed at each canard attachment point, and structural displacements were measured using attitude estimation by the IMU. In addition to the IMU, the aircraft was equipped with a GPS, a barometric altimeter and a geomagnetic sensor. The observations of each sensor estimated the position and attitude values and sensor bias. These flight controllers were integrated into a small UAV and Hardware In the Loop, and flight tests were conducted to validate these algorithms. Flight tests were conducted on this experimental aircraft. In this flight test, the gain of the PID control was changed during the flight, and the changes in response were compared. The introduction of integral control was able to burn out the steady-state pitch angle error that had occurred in flight.

Keywords: Flight Test, Active Aeroelastic Control, HILS, UAV

1. Introduction

High-altitude pseudo-satellites (HAPS), unmanned aerial vehicles that can fly day and night, are expected to complement and replace some of the functions of satellites in modern society. In particular, the functions of HAPS as radio communication stations and remote sensing platforms are expected to be superior to those of satellites in terms of both resolution and coverage due to their low cost and distance to the earth's surface.
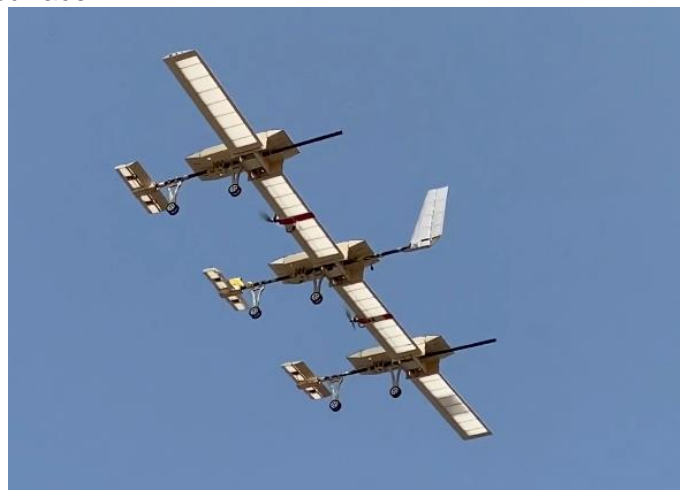

Figure 1 -- Experimental aircraft for active aeroelastic control

Recent progress in solar panel technology, battery technology and motor manufacturing technology has led to the recent development of fixed-wing HAPS using solar panels and batteries. However, at the current level of technology, it is challenging to operate fixed-wing HAPS without latitudinal and seasonal restrictions. To remove these restrictions, it is necessary to develop aircraft of unrealistic size. Some of the developed aircraft have wingspans of up to approximately 80 m. A smaller size is essential to achieve the low cost and enhanced operational flexibility of HAPS.

To achieve a smaller HAPS, the battery consumption in flight must be reduced. This requires the establishment of an unmanned aircraft with lightweight and elongated wings to reduce the drag generated by the wing. To answer this scientific question, the author has focused on active aeroelastic control technology, which stabilises and changes the deformation of a flexible structure by control so that even a structure with low strength can be used as a wing. This research aimed to predict and measure the wing's structural displacement in flight and extract the technology required for this active aeroelastic control. For this purpose, numerical simulations must be created, and actual aircraft data must be obtained by flying the technology demonstration aircraft.

This research aims to integrate actual aircraft data with numerical calculations. Developing a technical demonstration aircraft in which active aeroelastic control is implemented is necessary. There are few flight examples of experimental flexible aircraft in the world, with representative examples being the X-HALE[1] flight tests by Cesnik et al. and NASA's X-53[2] and X-56A[3] research results. When testing flexible aircraft, the following points must be considered from the early stages of design, which makes actual flight difficult: first, stability analysis for rigid aircraft can easily be thrown off balance by flexibility; second, not only the position of the centre of gravity but also the weight distribution of the entire airframe must be considered; third, due to the above characteristics, it is essential to develop a dynamics analysis program that takes flexibility into account. In particular, the authors' experimental aircraft shown in Figure 1 has an aircraft configuration with multiple canards for the reasons described below. Canards destabilise the aircraft, making it challenging to guarantee stability, and no flight examples of aircraft with multiple canards have been reported for flexible aircraft. This paper describes the details of this experimental aircraft's structural design, circuit system design, and control system design with multiple canards and the application of the numerical results to the actual aircraft.

2. Mathematical Modelling of flexible aircraft

2.1 Formularisation

There are various modelling approaches to flexible aircraft. For example, some model the wing by dividing it into several spring-mass-dampers, and others model it as several aircraft coupled together. Still, the method considered here discretises and numerically integrates the partial differential equations for the structural vibration to obtain the structural displacements. Modal analysis is commonly used to discretise the variational differential equations of the structure. Still, the authors developed a direct collocation method based on the pseudo spectral method and implemented it in MATLAB/Simulink.

To calculate the dynamic vibrations of a structure, it is necessary to solve the partial differential equations for structural dynamics. Neglecting the coupled terms of torsion and bending, the partial differential equations for bending and torsion are as follows. v is the bending and w is the twisting. EI_z and GI_p are stiffness of the structure and y is the spanwise position. F and T are distributed force and torque. σ is the cross-sectional density and J is the moment of inertia.

$$\sigma \frac{\partial^2 v}{\partial t^2} = \frac{\partial^2}{\partial y^2}\left(EI_z \frac{\partial^2 v}{\partial y^2}\right) + F(t, y) \tag{1}$$

$$J \frac{\partial^2 w}{\partial t^2} = \frac{\partial}{\partial y}\left(GI_p \frac{\partial w}{\partial y}\right) + T(t, y) \tag{2}$$

Boundary conditions are as follows.

$$v|_{root} = 0 \tag{3}$$

$$\left.\frac{\partial v}{\partial y}\right|_{root} = 0 \tag{4}$$

$$\left.\frac{\partial^2 v}{\partial y^2}\right|_{tip} = 0 \tag{5}$$

$$\left.\frac{\partial^3 v}{\partial y^3}\right|_{tip} = 0 \tag{6}$$

$$w|_{root} = 0 \tag{7}$$

$$\left.\frac{\partial w}{\partial y}\right|_{tip} = 0 \tag{8}$$

Modal analysis is a standard method for solving the above partial differential equations. Still, direct discretisation is more convenient when dealing with concentrated forces due to the multiple canards and distributed forces that vary according to the state quantities, as in the present study. Therefore, the authors have proposed a method for discretising partial differential equations using the Pseudo Spectral method[4], a type of Direct Collocation method. Consider a piecewise polynomial satisfying the above partial differential equation, where $\boldsymbol{\omega}$ is the coefficient vector of the piecewise polynomial.

$$v_{pol}^i(\tau) = \begin{pmatrix} 1 & \tau & \cdots & \tau^{N_i+1} \end{pmatrix}\boldsymbol{\omega_v} \tag{9}$$

$$w_{pol}^i(\tau) = \begin{pmatrix} 1 & \tau & \cdots & \tau^{N_i+1} \end{pmatrix}\boldsymbol{\omega_w} \tag{10}$$

The Pseudo-Spectral method is characterised by placing these spanwise positions τ according to an applicable rule. In this work, the node arrangement is based on the Legendre-Gauss-Radau node scheme[5]. The degree of the partition polynomial can be chosen to be less than 2n-1 degree, which guarantees the accuracy of the Gaussian quadrature. Still, because of the boundary conditions described below, it is necessary to set the number of boundary conditions not to exceed the total number of polynomial coefficients in all the sections.

In solving partial differential equations using polynomial interpolation, such as the Pseudo-Spectral method, it is essential to suppress the Runge phenomenon, which is an oscillation near the end of the interpolating polynomial. Therefore, to obtain a smooth curve, the integral of the square of the second-order derivative, which is the strain energy of the curve, is used as an evaluation function to calculate the coefficients of this polynomial. The definite integral of the strain energy of the curve can be directly written down in a quadratic form concerning the vector of coefficients of the polynomial. The strain energies are described as follows.

$$E_v = \int \left(\frac{\partial^2 v}{\partial \tau^2}\right)^2 d\tau \tag{11}$$

$$E_w = \int \left(\frac{\partial^2 w}{\partial \tau^2}\right)^2 d\tau \tag{12}$$

We consider applying this integral to a polynomial. The coefficients of the second-order derivative of the polynomial to be obtained are

$$\frac{\partial^2 v_{pol}^i(\tau)}{\partial \tau^2} = \begin{pmatrix} (N_i + 1)N_i\tau^{N_i-1} & N_i(N_i - 1)\tau^{N_i-2} & \cdots & 0 \end{pmatrix}\boldsymbol{\omega_v}. \tag{13}$$

Hence, the second power of the above equation is

$$\left(\frac{\partial^2 v_{pol}^i(\tau)}{\partial \tau^2}\right)^T \left(\frac{\partial^2 v_{pol}^i(\tau)}{\partial \tau^2}\right)$$

$$= \boldsymbol{\omega_v^T}\begin{pmatrix} (N_i + 1)N_i\tau^{N_i-1} & N_i(N_i - 1)\tau^{N_i-2} & \cdots & 0 \end{pmatrix}^T \begin{pmatrix} (N_i + 1)N_i\tau^{N_i-1} & N_i(N_i - 1)\tau^{N_i-2} & \cdots & 0 \end{pmatrix}\boldsymbol{\omega_v} \tag{14}$$

If we analytically calculate this in a definite integral at -1≤τ≤1, we obtain

$$E_v = \boldsymbol{\omega_v^T}E_{pol}\boldsymbol{\omega_v} \tag{15}$$

3

$$E_{pol} = \begin{pmatrix} \dfrac{(N_i+1)N_i(N_i+1)N_i}{(N_i-1)(N_i-1)} - (-1)^{(N_i-1)(N_i-1)+1}\dfrac{(N_i+1)N_i(N_i+1)N_i}{(N_i-1)(N_i-1)} & \cdots & 0 \\ \vdots & \ddots & \vdots \\ 0 & \cdots & 0 \end{pmatrix} \quad (16)$$

From the above, finding the vector of coefficients of a piecewise polynomial is attributed to the quadratic programming problem of minimising the strain energy under the equality constraint. From Lagrange multiplier method, we obtain

$$\begin{bmatrix} E_{pol}+E_{pol}{}^T & c_1^T & c_2^T & c_3^T & c_4^T & c_5^T \\ c_1 & & & & & \\ c_2 & & & & & \\ c_3 & & & 0 & & \\ c_4 & & & & & \\ c_5 & & & & & \end{bmatrix}\begin{bmatrix} \boldsymbol{\omega} \\ \lambda_1 \\ \lambda_2 \\ \lambda_3 \\ \lambda_4 \\ \lambda_5 \end{bmatrix} = \begin{bmatrix} \mathbf{0} \\ \boldsymbol{v} \\ v_0 \\ \mathbf{0} \\ CF \\ \mathbf{0} \end{bmatrix} \quad (17)$$

Here

c_1 : Condition that the polynomial passes through the interpolation point.
c_2 : Origin of deflection.
c_3 : Boundary conditions for wingtips and wing roots.
c_4 : Connection conditions for concentrated loads.
c_5 : connection conditions between each segment polynomial

This inverse matrix problem can be solved against $\boldsymbol{\omega}$ and multiplied by a matrix representing the analytic derivative of the polynomial to obtain the derivative matrix D. For example, the first-order derivative matrix is

$$D_{1v} = \begin{bmatrix} (N_i+1)\tau_0^{N_i} & N_i\tau_0^{N_i-1} & \cdots & 0 \\ & \vdots & & \\ (N_i+1)\tau_{N_i}^{N_i} & N_i\tau_{N_i}^{N_i-1} & \cdots & 0 \end{bmatrix}\omega \quad (18)$$

The differential matrix for calculating polynomial derivatives of arbitrary dimension.

$$\frac{\partial^n \boldsymbol{v}}{\partial y^n} = D_{nv}\boldsymbol{v} \quad (19)$$

$$\frac{\partial^n \boldsymbol{w}}{\partial y^n} = D_{nw}\boldsymbol{w} \quad (20)$$

Using this to discretise the partial differential equation, we get

$$\frac{\partial^2 \boldsymbol{v}}{\partial t^2} = D_{4v}\boldsymbol{v} + \boldsymbol{F} \quad (21)$$

$$\frac{\partial^2 \boldsymbol{w}}{\partial t^2} = D_{4w}\boldsymbol{w} + \boldsymbol{T} \quad (22)$$

Distributed force $\boldsymbol{F}$ and distributed torque $\boldsymbol{T}$ in equations (15) and (16) correspond to the lift and moment on the wing, respectively. The combined aircraft equation of motion is the small-disturbance equation of motion and is completed as a linear state-space representation. Therefore, the equations of motion for $\boldsymbol{F}$ and $\boldsymbol{T}$ are linearised in terms of the disturbance velocity, angle of attack, sideslip angle and angular velocity of each axis and included in the state-space representation.

2.2 Results of the Analysis
Numerical simulation investigates the roll angle control response of three tail fins positioned behind the main wings (Figure 2) and three canards in front of the main wings (Figure 3). Additionally, comparisons

are made between high and low wing stiffness, specifically between large and small diameters of the wing spars. Calculations are carried out for the four options listed in Table 1, each using simplified proportional roll angle control, and the responses are compared. The setpoint of the proportional roll angle control is fixed at 0.05 rad, the proportional gain from the roll angle to the left and right actuator angles is 1.59, and the simulation time is 20 s. The simulation is carried out using a simplified proportional roll angle control method. It is assumed that no wind disturbance is considered, the pitch angle is not controlled, and the velocity is controlled by appropriate PID control to reach the trim speed of 10 m/s.

In other common settings, the aircraft's weight is 4 kg, the span to 4 m and the design flight velocity to 10 m/s. Further details of the wing design included a rectangular wing with a wing string length of 0.2 m and an airfoil of S7055. The wing structure is assumed to be a single-spar structure with spars and ribs, and the main spar is considered to be made of a CFRP pipe with a wall thickness of 1 mm.

The results are shown in Figure 4 to Figure 7. Comparing the normal 1 with reduced wing stiffness and the multiple canard 1, the roll angle response of the normal 1 is slower, and the reverse response of the aileron occurs immediately after the start of the simulation. The cause of this reverse response is thought to be the roll moment caused by the lift force of the tail wing itself. In other words, before the actuator twists the main wing, the lift of the tail fin generates a moment that tries to roll the aircraft in the opposite direction. These are thought to cancel each other out, resulting in a slow roll response. This is particularly noticeable in the normal 2, where the roll moment due to tail lift is greater than the roll moment due to wing twisting, causing the ailerons to work in reverse. In contrast, the direction of the roll moment due to canard lift coincides with the direction of the roll moment due to wing twisting, resulting in a relatively straightforward roll characteristic. The roll characteristics of the normal configuration depend very strongly on the torsional stiffness of the main wings, and the design must be carried out with care to avoid inverse motions. In contrast, the multiple canard configuration has straightforward roll characteristics, and a relatively fast roll response can be expected even if the span is increased. Based on the above, multiple canards were adopted as the basic concept of the aircraft in this study.

Table 1 -- Configurations of numerical model

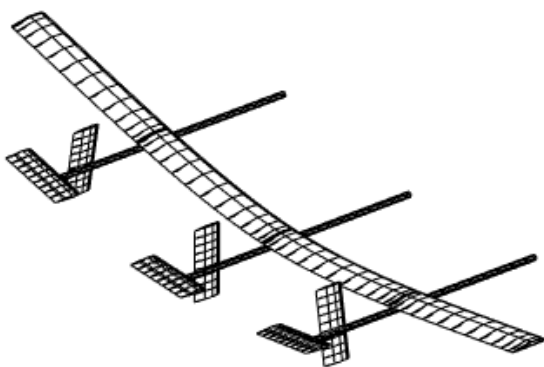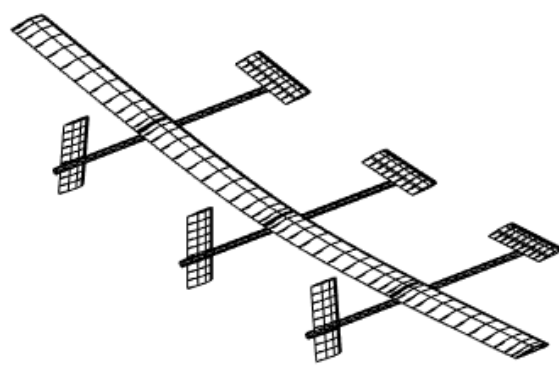| Name	Tail fin position	Spar Dia.
Normal 1	0.7m fore from L. E	10mm
Normal 2	0.7m fore from L. E	16mm
Multiple canard 1	0.7m aft from L. E	10mm
Multiple canard 2	0.7m aft from L. E	16mm

Figure 2 – Normal configuration
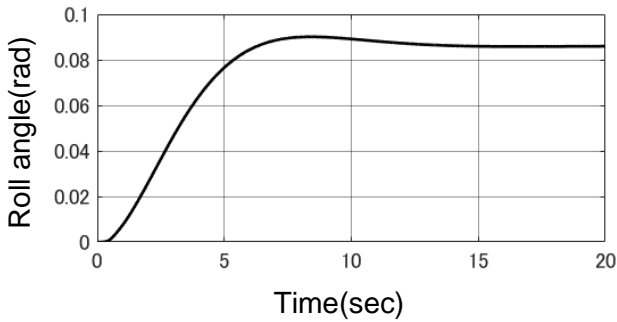

Figure 3 – Multiple canards configuration

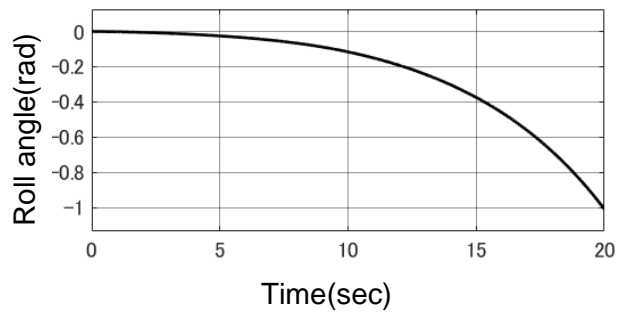Figure 4 – Roll Response of Normal 1
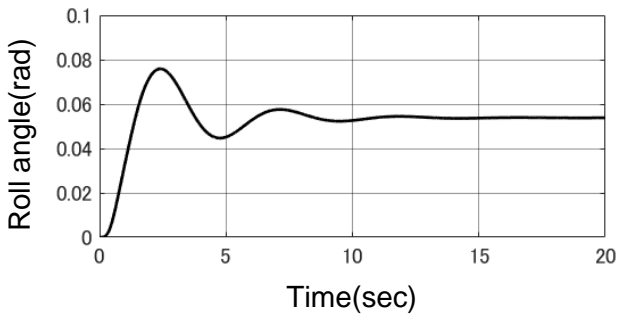
Figure 5 – Roll Response of Normal 2

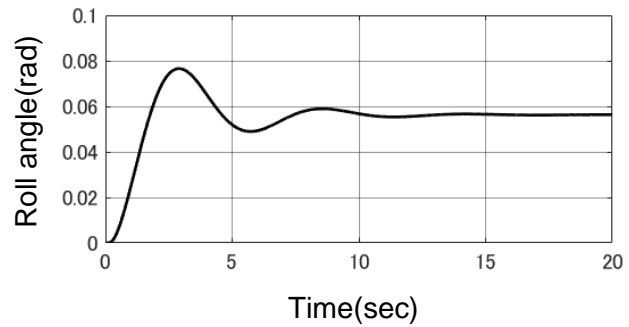Figure 6 – Roll Response of Multiple canard 1

Figure 7 – Roll Response of Multiple canard 2

3. Design and Development of Multiple Canard Aircraft with Span 4m

In the design, we considered ensuring high rigidity for a flexible aircraft, so that linearity in structural deformation could be confirmed. In addition, components were standardised as far as possible to facilitate the replacement of parts even if the aircraft was damaged in a crash. Similarly, the circuit and control systems were made as common as possible in each fuselage to make manufacturing and replacing parts more accessible. As a safety issue during flight, the circuit system has a backup system that enables the actuators to operate using only the signals from the radio transmitter, ignoring all controls, etc., regardless of the state of the microcomputer. In a control system failure, it is possible to manually land or takes the aircraft to a safe zone.

3.1 Aerodynamic Design of the Aircraft

The aerodynamic design concept was to keep it simple, except for the elements required to verify active aeroelastic control. The wings are all rectangular, and a flat-bottomed airfoil was also selected to select the airfoil shape, prioritising manufacturability. The top view and the cross-sectional shape of the airfoil are shown in Figure 8 and Figure 9.

The aerodynamic design procedure involved determining the size of the aircraft and wings using the previously mentioned structure-motion coupled analysis programme, then assuming that the aircraft was rigid, aerodynamic and dynamic stability analyses were carried out using the open-source aerodynamic analysis programme XFLR5[6] shown in Figure10. The structural vibration was again confirmed using the coupled structure-motion analysis programme.
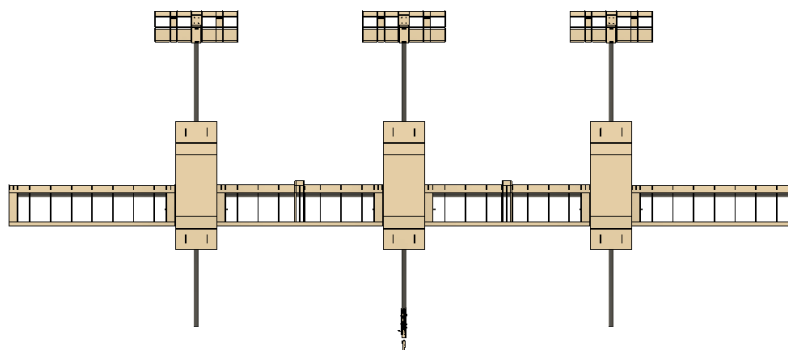
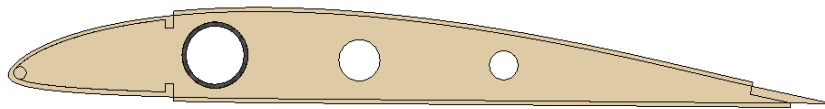Figure 8 -- Top view of this experimental aircraft

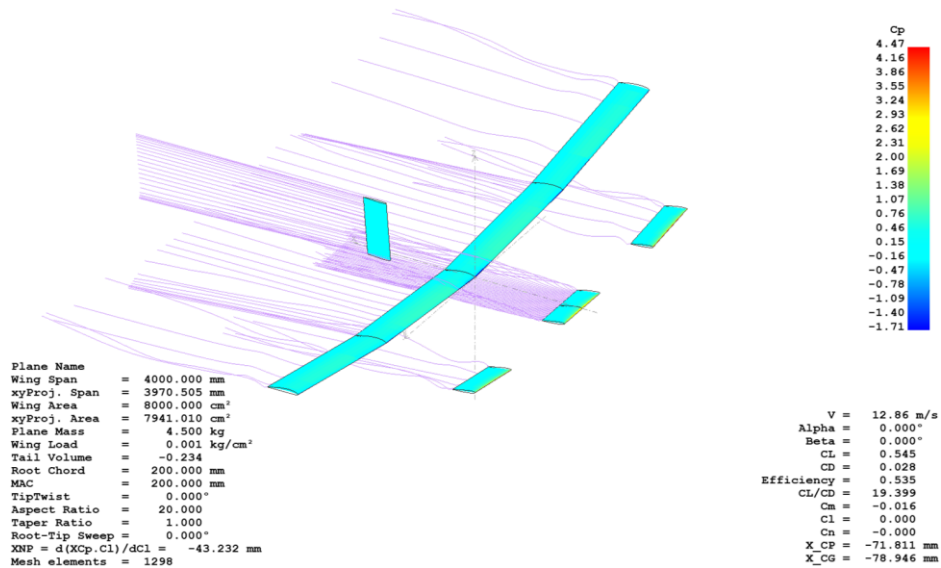Figure 9 – Wing cross-section view of this experimental aircraft


```
Plane Name
Wing Span       =   4000.000 mm
xyProj. Span    =   3970.505 mm
Wing Area       =   8000.000 cm²
xyProj. Area    =   7941.010 cm²
Plane Mass      =      4.500 kg
Wing Load       =      0.001 kg/cm²
Tail Volume     =     -0.234
Root Chord      =    200.000 mm
MAC             =    200.000 mm
TipTwist        =      0.000°
Aspect Ratio    =     20.000
Taper Ratio     =      1.000
Root-Tip Sweep  =      0.000°
XNP = d(XCp.Cl)/dCl =   -43.232 mm
Mesh elements   =   1298
```

```
        V =    12.86 m/s
    Alpha =     0.000°
     Beta =     0.000°
       CL =     0.545
       CD =     0.028
Efficiency =     0.535
    CL/CD =    19.399
       Cm =    -0.016
       Cl =     0.000
       Cn =    -0.000
     X_CP =   -71.811 mm
     X_CG =   -78.946 mm
```

Figure 10 – XFLR5 analysis of this experimental aircraft

3.2 Structural Design of the Aircraft

In the structural design, the highest priority was the ease of construction. For the structural style of the wing, a rigidity calculation was made in the form of a single spar structure to facilitate the analysis of the stiffness. Figure 11 shows the design diagram of the wing. The stiffness of the skin was also considered, but the size of the skin was kept to a minimum, as its contribution to the torsional stiffness was too large. In contrast, too large a torsional stiffness would counteract the maneuverability advantages of multiple canards. The fuselage structure was constructed entirely of a balsa. Figure 12 shows the fuselage design. This fuselage had a large frontal area, and test flights indicated huge aerodynamic drag, so the next aircraft with a smooth fuselage shown in Figure 13 is currently under construction.
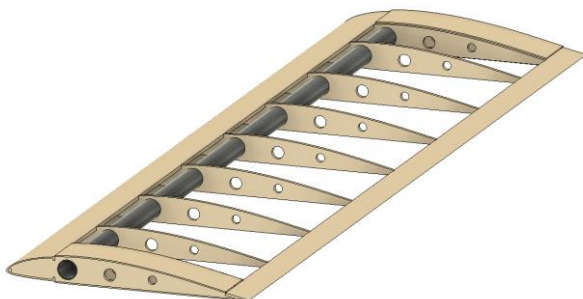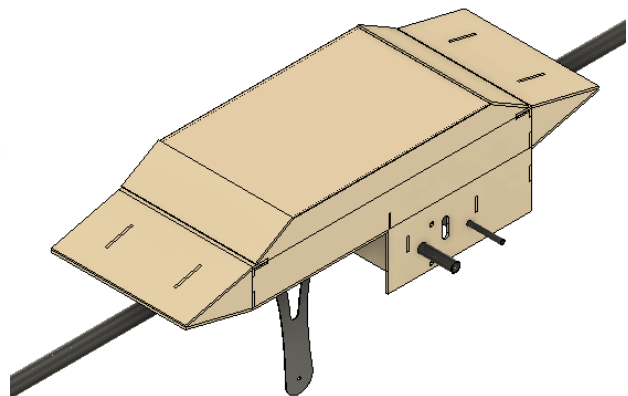

Figure 11 – Structural design of the wing

Figure 12 – Structural design of a fuselage

Figure 13 – Design of next experimental aircraft

3.3 Circuit Design of the Aircraft

A connection diagram of the circuit system design is shown in Figure 14. UART carried out the communication between each board, so two communication lines connected the Log board and each Tail board. In addition, PWM signals supplied by a commercially available receiver were distributed to each board to build the backup system described above. The SBUS signal used for controlling the canard deflection was converted to the usual UART format by an inverting circuit on the board and then distributed to each Tail board.

The boards were designed using AutoCAD's EAGLE and manufactured by cutting the boards using CNC. The fabricated boards are shown in Figure 15. LAN cables and modular jacks, which are easily available and do not require caulking, were used to connect the boards. The microcomputer used for the calculation is an STM32F767ZI evaluation board so that the microcomputer can be easily replaced or modified later. It is also possible to perform calculations integrating all information on the Log board, in which case inter-board communication is used to give instructions to the actuators respectively.
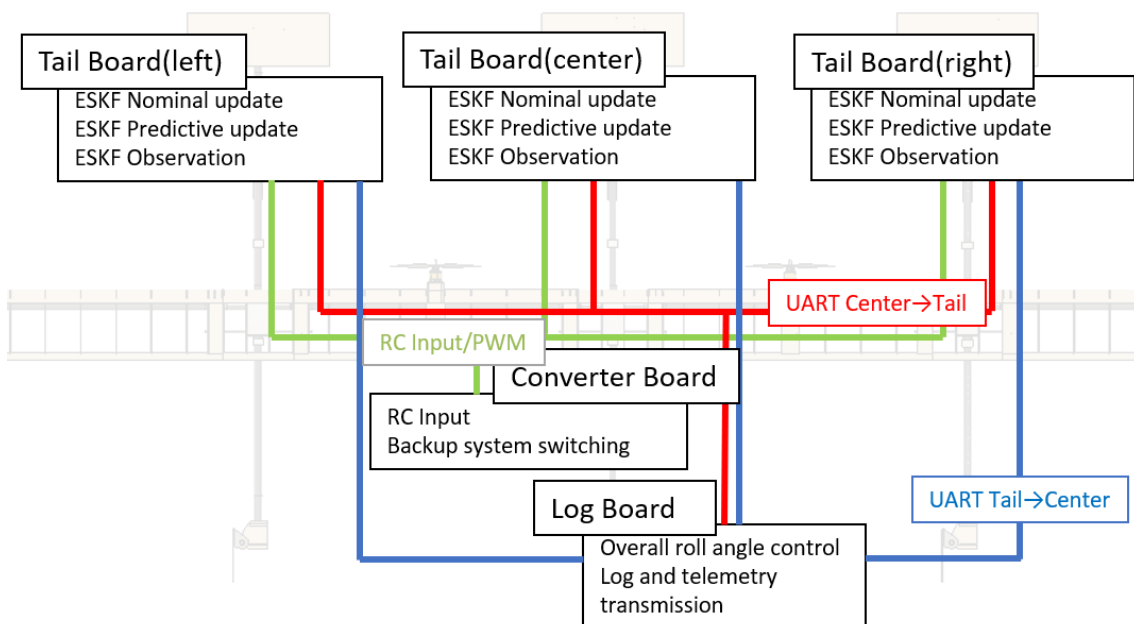

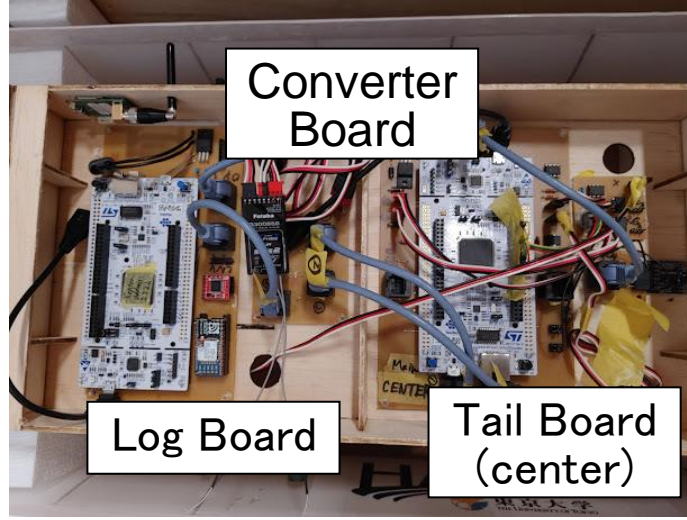Figure 14 – Connection diagram of the experimental aircraft

Figure 15 – the board layout in fuselage (centre)

3.4 Attitude Estimation and Control of Aircraft

3.4.1 Attitude Estimation

This experimental aircraft estimates the attitude angle in each fuselage and treats the difference as structural displacement. Highly accurate attitude estimation is therefore essential to accurately capture structural displacement. For attitude estimation, information from MEMS gyro-sensors and GPS was integrated using a Kalman filter to estimate position, velocity, attitude, and each sensor's bias. The Kalman filter used was an Error State Kalman Filter (ESKF) [7].

3.4.2 Error State Kalman Filter

First, the aircraft's attitude is represented using Quaternion as a coordinate transformation from the NED coordinates to the aircraft coordinates.

$$q = \begin{bmatrix} q_w \\ \boldsymbol{q_v} \end{bmatrix} \tag{23}$$

The Error State Karman Filter divides nominal state update, which integrates the gyro sensor output, including errors, and error state update, which is the integration of errors. Only the axial error component q_e of the error Quaternion, $\boldsymbol{q_e}$, is included in the state vector of the Karman Filter.

$$q = \hat{q} \times q_e \tag{24}$$

$$q_e = \begin{bmatrix} 1 \\ \boldsymbol{q_e} \end{bmatrix} \tag{25}$$

Here, $\hat{q}$ is the attitude angle obtained by integrating the quaternion integral of the gyro sensor output as it is, and q_e is the error quaternion. The Error state quantities are integrated into the nominal state quantities as appropriate, to prevent them from becoming so large that they deviate from the approximation of the error state quantities. We define a nominal state quantity vector x, an error state quantity vector δx, an input vector u_m and a perturbation vector i. p_n is the position vector in NED coordinates, v_n is the velocity vector, a_b is the bias error in each axis of the accelerometer, ω_b is the bias error in each axis of the gyro sensor and g is the gravitational acceleration vector. Details and other nomenclature are shown in reference [7].

$$x = \begin{bmatrix} p_n \\ v_n \\ q \\ a_b \\ \omega_b \\ g \end{bmatrix}, \delta x = \begin{bmatrix} \delta p_n \\ \delta v_n \\ \delta\theta \\ \delta a_b \\ \delta\omega_b \\ \delta g \end{bmatrix}, u_m = \begin{bmatrix} a_m \\ \omega_m \end{bmatrix}, i = \begin{bmatrix} v_i \\ \theta_i \\ a_i \\ \omega_i \end{bmatrix} \tag{26}$$

The discretised equation of state for the state quantity is then

$$\delta x \leftarrow F_x(x, u_m)\delta x + F_i i \tag{27}$$

9

The estimation equation for the error state quantity is expressed as follows

$$\widehat{\delta x} \leftarrow F_x(x, u_m)\delta x \tag{28}$$

$$P \leftarrow F_x P F_x^T + F_i Q_i F_i^T \tag{29}$$

Here,

$$F_x = \begin{bmatrix} I & I\Delta t & 0 & 0 & 0 & 0 \\ 0 & I & -R[a_m - a_b]_\times & -R\Delta t & 0 & I\Delta t \\ 0 & 0 & R^T\{(\omega_n - \omega_b)\Delta t\} & 0 & -I\Delta t & 0 \\ 0 & 0 & 0 & I & 0 & 0 \\ 0 & 0 & 0 & 0 & I & 0 \\ 0 & 0 & 0 & 0 & 0 & I \end{bmatrix} \tag{30}$$

$$F_i = \begin{bmatrix} 0 & 0 & 0 & 0 \\ I & 0 & 0 & 0 \\ 0 & I & 0 & 0 \\ 0 & 0 & I & 0 \\ 0 & 0 & 0 & I \\ 0 & 0 & 0 & 0 \end{bmatrix} \tag{31}$$

$$Q_i = \begin{bmatrix} V_i & 0 & 0 & 0 \\ 0 & \theta_i & 0 & 0 \\ 0 & 0 & A_i & 0 \\ 0 & 0 & 0 & \Omega_i \end{bmatrix} \tag{32}$$

Observations of the ESKF included position and velocity observations using GPS and barometric sensors and azimuth and gravity direction observations; for GPS and azimuth observations, see references [7] and [8]. Observations of the direction of gravity were made by

$$H_{\delta x} = \begin{bmatrix} 0 & 0 & [R^T g]_\times & -I & 0 & R^T \end{bmatrix} \tag{33}$$

$$\delta x \leftarrow K(-a_m - R^T g) \tag{34}$$

$$K = P H_{\delta x}^T \left(H_{\delta x} P H_{\delta x}^T + V\right)^{-1} \tag{35}$$

$$P \leftarrow (I - K H_{\delta x})P \tag{36}$$

The coincidence of the accelerometer output and the gravity vector is treated as an observation. If the covariance matrix V in the observation is too small, the attitude error due to the dynamic acceleration of the aircraft increases.

3.4.3 HIL Verification and Flight Testing with a Small Unmanned Aerial Vehicle

The attitude estimation algorithm described above was implemented, and the avionics of the experimental aircraft was developed. Still, it was decided that the risk of crashes due to circuit and software faults was too high to immediately mount the produced algorithm on this experimental aircraft and fly it. To minimise the risk of defects, the circuit and control system were verified by mounting them on a small unmanned aerial vehicle and conducting Hardware In the Loop simulations and actual flight tests. This section first describes the HIL by numerical simulation and then describes the results of the validation and reliability of the HIL by flight tests.

An overview of the small unmanned aircraft to be used is shown in Figure 16. The aircraft is a tailless aircraft with an approximately 0.9 kg and a span of 1.2 m. The aerodynamic derivative coefficients were calculated using the stability analysis of the aerodynamic analysis software XFLR5 [5]. In contrast, the lift, drag and moment coefficients were calculated for the angle of attack, respectively, and the aerodynamic coefficients were obtained by cubic spline completion of the obtained graph. The analysis screen is shown in Fig. 17, and the values of the aerodynamic derivative coefficients are in Table 2.Table 3 shows the equipped parts in the avionics.

Table 2 -- Reference and Coefficients

Reference	Value
Area	0.421 m^2
Cref	0.253 m
Bref	1.2 m
Derivatives Coefficients	
C_{ma}	-0.405
C_{mq}	-1.620
C_{Yb}	-0.189
C_{Yp}	-0.135
C_{Yr}	0.176
C_{lb}	-0.136
C_{lp}	-0.284
C_{lr}	0.101
C_{nb}	0.064
C_{np}	-0.006
C_{nr}	-0.054

Table 3 -- Equipped parts

Component	Model Number
Microcomputer	STM32F767ZI
Accelerometer	
Gyro sensor	Pmod Nav
Geomagnetic sensors	(LSM9DS1+LPS25HB)
Barometric pressure sensor	
GPS receiver	Pre-GO 9T (u-blox ZED-F9T)
SD card writer	Open Log
Telemetry	TWELITE DIP
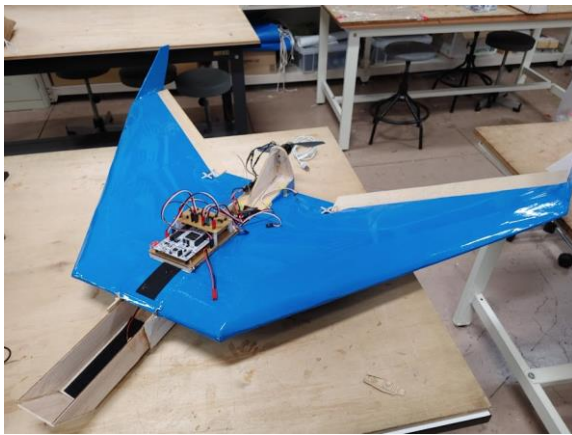
Figure 16 – Overview of the small UAV
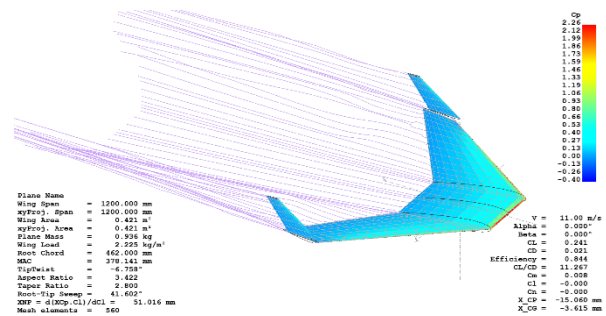
Figure 17 – XFLR5 analysis of small UAV

Hardware In the Loop (HIL) is a simulation that directly connects the simulator to the aircraft avionics and simulates the real flight environment by estimating the attitude and determining the control amount for the sensor signals generated by the simulator, using the control amount as input to the simulator. The simulator was developed in-house. X-Plane was used to visualise the state of the aircraft, and NASA's XPlaneConnect [9] was used to connect the simulator to X-Plane.

The actual values of the quantities measured by each sensor were sent from the simulator to the avionics via UART(Figure 18), and the noise was added inside the avionics. The noise of the sensors onboard the aircraft was determined and used for the sensor noise. The simulation results are shown in Figure 19, where the actual value of the attitude angle is shown as a blue dashed line since HILS provides the true value of the attitude angle. Immediately after the start of the flight, there is a maximum error of about 15 deg in the pitch angle and 25 deg in the roll angle, but both errors converge to about ±5 deg within 60 s after the start of the flight. This indicates that the parameter estimation by ESKF is working well. The flight test results are shown in Figures 20 and 21. Although the flight tests cannot be discussed quantitatively because actual values cannot be obtained, no serious discrepancies were observed compared to the flight movies. The flight tests were carried out without damage or malfunctions.
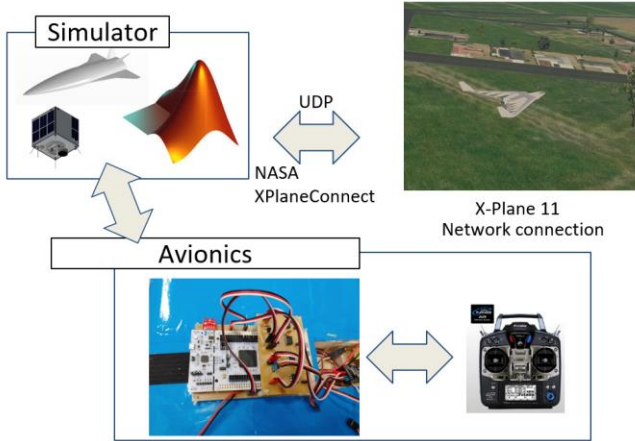
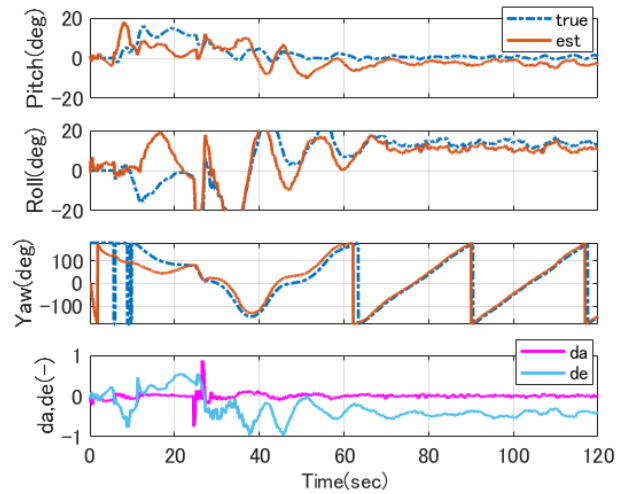Figure 18 – HIL configuration

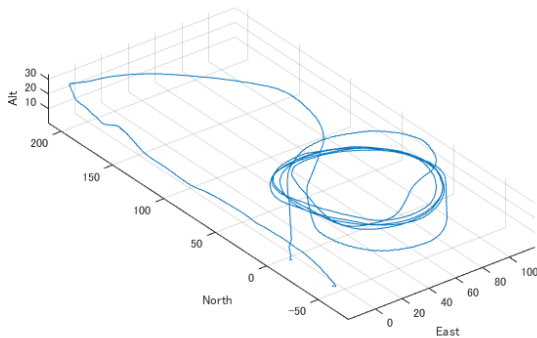Figure 19 – HIL simulation result

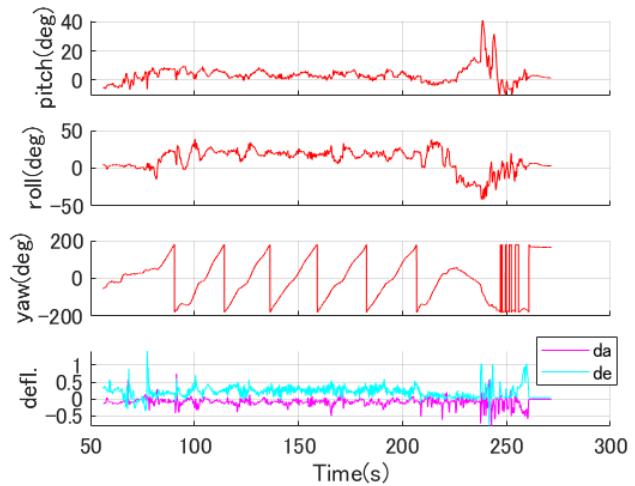
Figure 20 – Trajectory of the flight for small UAV

Figure 21 – Attitude estimation result

3.4.4 Attitude Control

Attitude control in this experimental aircraft used common PID control. Figure 22 shows the control diagram. The primary control is to make the pitch angle follow the specified value for the attitude estimated for each fuselage. The overall control of the aircraft was performed by varying these respective pitch angle specified values. The individual pitch angles varied uniformly concerning the RC inputs for overall pitch angle control. For the roll angle control, a target value for the average roll angle was generated from the RC input, and a target pitch angle for the left and right fuselage was generated from the PID controller concerning the average roll angle. In this way, the pitch angle of each fuselage was stabilised in a relatively quick period. Then the attitude control of the entire aircraft was performed as long-period guidance control.

The PID gains were adjusted by wind tunnel tests on each fuselage and calculated using the Ultimate Gain method. The details of these wind tunnel tests are omitted for reasons of paper limitation. The set gain values are shown in Table 4. The integral gain was made so that it could be switched during flight, as described below.
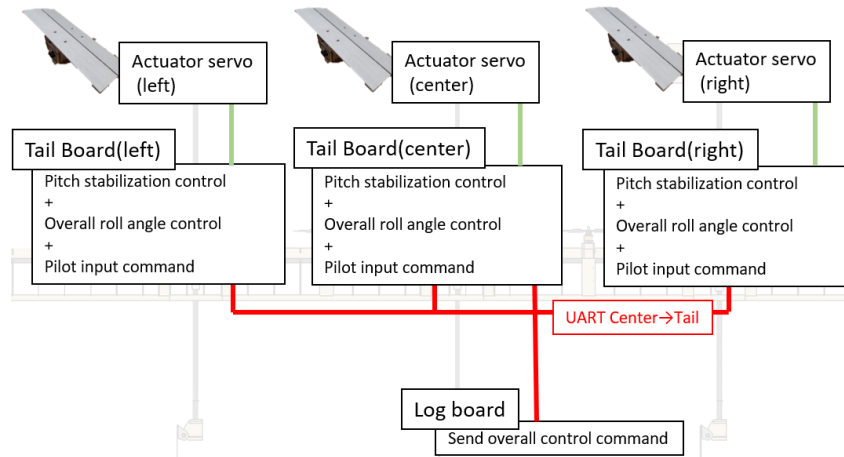
Figure 22 – Control diagram of the experimental aircraft

Table 4. PID Gain Value of the attitude control

PID Input	PID Output	P gain	I gain	D gain
Pitch angle	Actuator deflection (-1 to 1)	6.36	0.0 (5.300)	0.954
Roll angle	pitch setpoint difference	10.0	0.0	1.0
Yaw rate	Rudder deflection (-1 to 1)	2.0	0.0	0.0

4. Result of Flight Test

Figure 23 and 24 show the results of a test flight in which the I-gain value was changed in the flight. At 110 s after the start of logging, the I-gain was changed from 0 to 5.3 by a switch on the RC. As a result, the steady-state pitch angle error that occurred around 90 s after the start of logging was almost eliminated by 150 s after the start of logging, confirming the effect of the integral gain. However, from about 140 s after the start of logging, this steady-state error is counteracted by a large deflection angle, which is expected to increase resistance and reduce control performance. The reason for this steady-state error in pitch angle is thought to be due to a lack of adjustment of the weight distribution, and adjustments will be made in the future to prevent this large deflection angle from occurring.

No significant discrepancies were found when the results of the flight reproduction using the logs were compared with the actual flight movies.
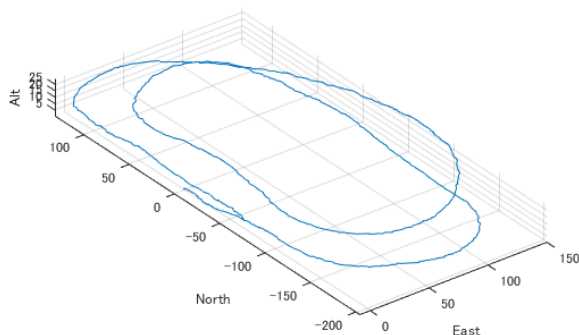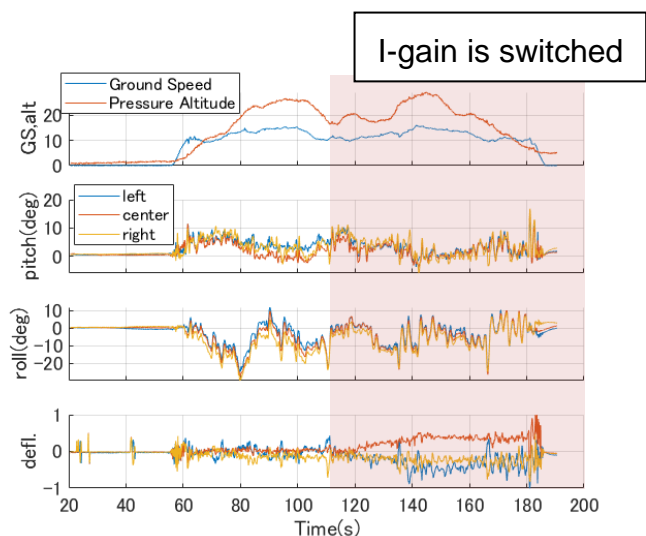

Figure 23 – Trajectory of the Flight test   --   Figure 24 – Attitude of the each fuselage

5. Conclusion

This paper describes the analysis carried out to design and build this experimental aircraft with active aeroelastic control, as well as the specific design work and test flight results. In the coupled structure-motion analysis, the roll response characteristics revealed the advantages of the multiple canard configuration. In the specific design of this experimental aircraft, the control system was carefully designed in particular. To verify this, HIL simulations and flight tests were conducted using a small unmanned aerial vehicle to confirm the validity of the algorithms for attitude estimation, etc.

In the flight tests of this experimental aircraft designed according to the above procedure, a steady flight was successfully achieved and the control gains were changed during the flight. In the future, various validations will be carried out using this experimental aircraft.

6. Contact Author Email Address

naoto-morita@g.ecc.u-tokyo.ac.jp

7. Copyright Statement

The authors confirm that they, and/or their company or organization, hold copyright on all of the original material included in this paper. The authors also confirm that they have obtained permission, from the copyright holder of any third party material included in this paper, to publish it as part of their paper. The authors confirm that they give permission, or have obtained permission from the copyright holder of this paper, for the publication and distribution of this paper as part of the ICAS proceedings or as individual off-prints from the proceedings.

Acknowledgments

References

[1] Cesnik, C. E., Senatore, P. J., Su, W., Atkins, E. M., and Shearer, C. M. X-HALE: A very flexible unmanned aerial vehicle for nonlinear aeroelastic tests. *AIAA journal*, Vol. 50, No. 12, pp 2820-2833,2017.

[2] Pendleton, E., Flick, P., Paul, D., Voracek, D., Reichenbach, E., and Griffin, K. The X-53 A summary of the active aeroelastic wing flight research program. *48th AIAA/ASME/ASCE/AHS/ASC Structures, Structural Dynamics, and Materials Conference,* pp 1855,2007.

[3] Burnett, E. L., Beranek, J. A., Holm-Hansen, B. T., Atkinson, C. J., & Flick, P. M. Design and flight test of active flutter suppression on the X-56A multi-utility technology test-bed aircraft. The Aeronautical Journal,Vol. 120, No. 1228, pp 893-909, 2016

[4] Fahroo, F., and Ross, I. M. Costate estimation by a Legendre pseudospectral method, *Journal of Guidance, Control, and Dynamics*, Vol. 24, No. 2, pp 270-277, 2001.

[5] Garg, D., Patterson, M., Hager, W. W., Rao, A. V., Benson, D. A., and Huntington, G. T. A unified framework for the numerical solution of optimal control problems using pseudospectral methods, *Automatica*, Vol. 46, No. 11, pp 1843-1851, 2010.

[6] Deperrois, A. XFLR5 Analysis of foils and wings operating at low Reynolds numbers. Guidelines for XFLR5, 2009.

[7] Sola, J. Quaternion kinematics for the error-state KF, *Laboratoire dAnalyse et dArchitecture des Systemes-Centre national de la recherche scientifique (LAAS-CNRS)*,2012.

[8] Meier, L., Honegger, D., and Pollefeys, M. PX4: A node-based multithreaded open source robotics framework for deeply embedded platforms. *IEEE international conference on robotics and automation (ICRA),* pp 6235-6240, 2015

[9] Teubert, C.; Watkins, J. The X-Plane Connect Toolbox. https://github.com/nasa/XPlaneConnect